Reflectivity-based evaluation of the coalescence of two condensing drops and shape evolution of the coalesced drop

Shripad J. Gokhale,[1] Sunando DasGupta,[2] Joel L. Plawsky,[1,*] and Peter C. Wayner, Jr.[1,†]
[1]*The Isermann Department of Chemical and Biological Engineering, Rensselaer Polytechnic Institute, Troy, New York 12180, USA*
[2]*Department of Chemical Engineering, Indian Institute of Technology, Kharagpur, PIN 721302, India*
(Received 14 May 2004; revised manuscript received 25 August 2004; published 30 November 2004)

Image analyzing interferometry is used to study the details of the evolving shapes and coalescence of two condensing drops of 2-propanol on a quartz surface. The measured thickness profiles give fundamental insights into the transport processes within the drops before and after coalescence and the evolution of the coalesced drop from asymmetric to symmetric shape. The results indicate that the constant value of the adsorbed film thickness between the drops and profiles of the local thickness, slope angle, curvature, and curvature gradient govern the pressure fields in the coalescing drops. The shape evolution after coalescence is found to be driven by the capillary forces within the drop. Using the experimental data, we find that the calculations of the average shear stress for the fluid flow between the drops, the decrease in the interfacial excess energy, and the positions of the center of mass of the drops explain the physics of the coalescence phenomenon. However, the flow field is found to be complex because the pressure field indicates that there are complicated flows within the drop.

DOI: 10.1103/PhysRevE.70.051610 PACS number(s): 68.03.Cd, 47.55.Dz, 68.37.−d, 68.03.Fg

I. INTRODUCTION

The coalescence of drops is fundamental to the understanding of a wide range of applications such as ink jet printing, emulsion formation, oil recovery, polymer blending, phase change heat transfer in dropwise condensation, etc. Previous studies of this subject have mainly analyzed the dynamics and external flow fields during coalescence [1–3], draining of the thin film between the drops and the role of intermolecular interactions [4–9], and the kinetics of relaxation of the drop [1,2,10]. Andrieu *et al.* [1] experimentally observed the coalescence of water drops on a silane-modified glass surface and explained the observed relaxation time of the drops using a model based on the phase change near the contact line region. Menchaca-Rocha *et al.* [2] analyzed the effect of surface tension on the coalescence of mercury drops and compared their results with numerical calculations based on the Navier-Stokes equation. The effects of London–van der Waals forces, electrostatic interactions, and surface forces on the thinning of the film between the coalescing drops and on the coalescence time have been studied by Li [5], Deshikan and Papadopoulos [6], and Ivanov *et al.* [8]. Herein, we study experimentally the effects of the thickness, slope angle, curvature, apparent contact angle, and pressure fields in the contact line region, during low rates of condensation, on the shape evolution of condensing and coalescing drops due to capillary flow.

In the experimental system [Fig. 1(a)], two drops of a partially wetting fluid (2-propanol) grow on a quartz surface during condensation and coalesce when they touch. A schematic of a drop is sketched in Fig. 1(b). In a 1957 seminal paper, Derjaguin and Zorin [11] demonstrated that a thin adsorbed flat film of *n*-propyl alcohol became unstable at the saturation point at a film thickness of approximately 5.5 nm. Above this thickness, they viewed "microdewdrops" on an adsorbed layer. Therefore, the adsorption isotherm near the saturation point is very complex for a polar fluid [11]. The important process of dropwise condensation occurs in this region of the adsorption isotherm. The macroscopic observations of the condensing drops and the associated adsorbed

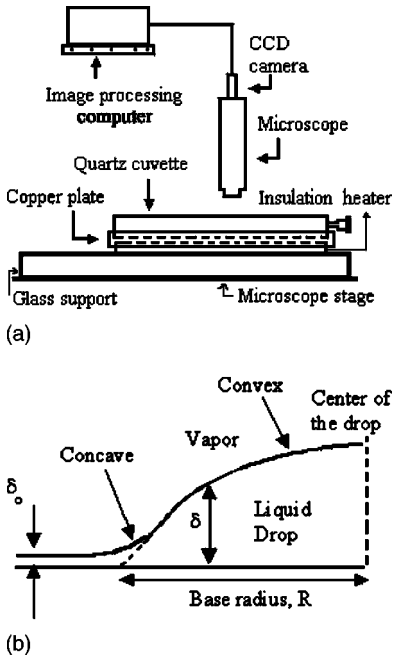

FIG. 1. (a) Schematic drawing of the experimental setup. (b) Schematic drawing of the cross section of a drop. δ is the film thickness along the profile of the drop, and δ_0 is the thickness of the flat adsorbed film adjacent to the drop.

*FAX: 518-276-4030. Electronic mail: plawsky@rpi.edu
†FAX: 518-276-4030. Electronic mail: wayner@rpi.edu

thin film reported herein are consistent with the work by Derjaguin and Zorin [11].

We measure the microscopic details of the defining characteristics (thickness profile and surrounding adsorbed film thickness) of the condensing drops. We study the growth and coalescence of these microdewdrops using high-resolution microinterferometry and an improved data analysis technique. There is a lack of experimental data concerning these details. An image analyzing technique based on the analysis of the reflectivity profiles [12–14] is used to obtain the profiles of the thickness, slope, and curvature of these drops, including the profiles in the contact line region. The results indicate that the slope angle, curvature, and curvature gradient govern the pressure fields in the coalescing drops. Although the contact line region was theoretically shown to govern the spreading of drops previously [15–19], to the authors' knowledge, there is no previous experimental study of the effects of the microscopic details of the shape profiles in the contact line region on the coalescence of two drops. Based on the experimental results, we calculate the driving force and the decrease in the interfacial free energy, which causes the coalescence process. The experimentally obtained contact line velocity during spreading, the slope angle (a measure of the apparent contact angle of the drop), and the curvature profiles explain how the coalescence occurs. Using the experimental data, we find that an average shear stress for the fluid flow between the drops explains the physics of the coalescence phenomenon. The resultant coalesced drop is initially asymmetric, and it relaxes towards a symmetric shape. The experimentally measured position of the center of mass of the coalesced drop is found to be closer to that of the larger drop, and the results agree with the theoretical calculations based on the two-dimensional analysis of drops by Andrieu *et al.* [1]. The shape evolution after coalescence is found to be driven by capillary forces within the drop. The pressure field within the coalesced drop, calculated from the curvature profile, the slope angle, and the intermolecular forces, explains how and why the drop shape evolves after coalescence.

II. EXPERIMENTAL SETUP AND PROCEDURES

A schematic diagram of the experimental setup is shown in Fig. 1(a). The experimental cell [13,14,20] consists of a UV-grade quartz cuvette with inside dimensions of 3 mm $\times$3 mm, outside dimensions 5.5 mm$\times$5.5 mm, and length 43 mm. The cuvette is cleaned with the working liquid (2-propanol from Sigma-Aldrich, Inc., purity 99.8%), dried in an oven at 150°C for 45 min and partially filled with liquid inside a controlled environment of nitrogen. The quartz cell is mounted axially on a copper plate, which is slightly heated from the bottom by an insulated flexible heater (from Omega Engineering, Inc.). Vapors of 2-propanol formed inside the quartz cell condense on the upper surface inside the cell, as it is at a slightly lower temperature. Since 2-propanol partially wets the quartz surface above a critical thickness, we observe dropwise condensation of 2-propanol and the mutual interaction of the drops on the top surface inside the cuvette. The entire setup is mounted on a microscope stage as shown in Fig. 1(a). The spreading of the drop results from the combined effects of liquid flow towards the contact line region due to the pressure gradient within the drop and the phase change (condensation) process occurring at the liquid-vapor interface of the drop.

An imaging technique called image analyzing interferometry (IAI) [12–14,19,21] based on the measured reflectivity of the liquid film at each pixel location along the entire drop profile relative to that of the calibrated bare surface (which corresponds to an adsorbed film thickness equal to zero) is used to measure the drop shape. Monochromatic light (λ =543.5 nm) from a Hg arc is used as the light source. Naturally occurring interference fringes result due to the reflection of light at the liquid-vapor and solid-liquid interfaces as demonstrated by the optical micrographs presented in Fig. 2. A charge-coupled-device (CCD) camera is used to capture the images of the reflectivity pattern of the drops. The captured images are digitized into 640$\times$480 pixels and assigned one of 256 possible gray values representing intensity from 0 (black) to 255 (white). We measure the liquid-vapor interfacial profile changes from convex in the thicker portion of the drop to concave in the thinner portion of the drop. The experimental technique also demonstrates the presence of a thin, flat adsorbed film associated with the condensing drops.

Imaging techniques giving fewer details have been used in the past to observe the interfacial phenomena in various systems. For example, Wiegand *et al.* [21] studied the wetting properties of micropatterned surfaces using this technique, but called it reflection contrast interferometry. Blake [22] used double-wavelength interferometry to investigate equilibrium wetting films of alkanes on α-alumina. Wayner and co-workers [12,13,20,23–29] used ellipsometry and interferometry techniques to study the liquid-vapor interfacial phenomena during phase change processes in both wetting and nonwetting systems. Chen and Wada [30] used laser interferometry to investigate microlayer spreading phenomena.

III. DATA ANALYSIS TECHNIQUE

The image analysis technique is described in detail in a related publication [14]. Only a brief description is given herein. From each image of the drop, a plot of the pixel gray value (G) versus pixel position (x) is extracted. A computer program scans the reflectivity pattern and calculates a relative gray value at each pixel position using

$$\overline{G}(x) = \frac{G(x) - G_{\min}(x)}{G_{\max}(x) - G_{\min}(x)}, \tag{1}$$

where $G_{\min}(x)$ and $G_{\max}(x)$ are the interpolatory envelopes to the various order minima and maxima (constructive and destructive fringes). Using the measured gray value of the bare surface of the cuvette (corresponding to zero film thickness) for calibration, the thickness (δ) at each pixel location is obtained from the relative gray value (RL) at that pixel location [14] using

$$\mathrm{RL}(x) = \overline{G}(x)[\mathrm{RL}_{\max} - \mathrm{RL}_{\min}] + \mathrm{RL}_{\min}, \tag{2}$$

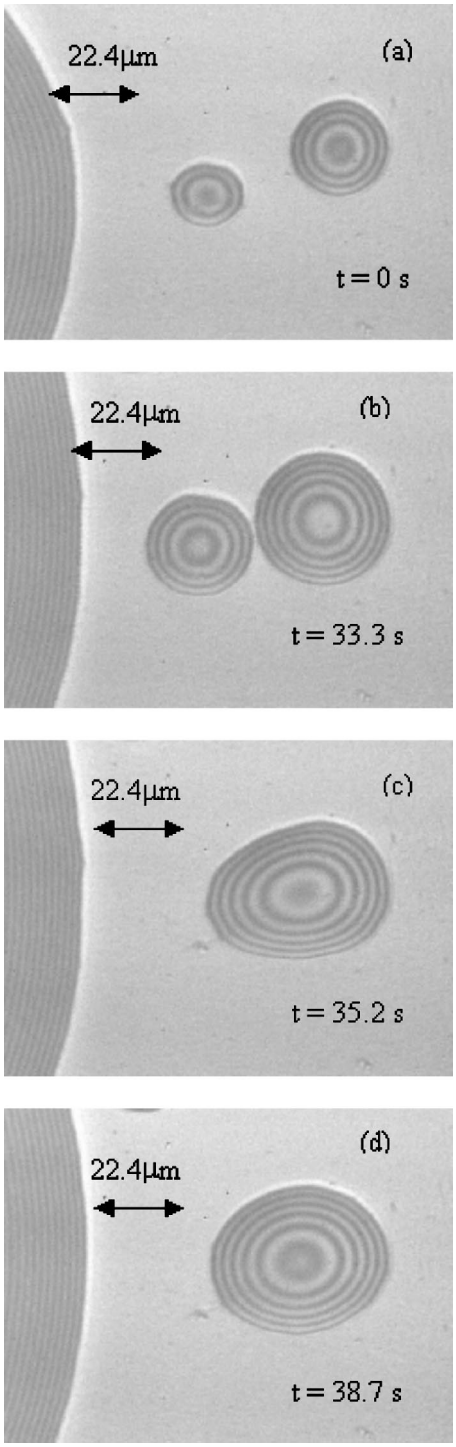

FIG. 2. Optical micrographs of the condensing drops during the coalescence process as a function of time.

$$\mathrm{RL} = \frac{\alpha + \beta \cos 2\theta_l}{\kappa + \beta \cos 2\theta_l}, \tag{3}$$

where

$$\theta_l = \frac{2\pi n_l \delta}{\lambda}, \quad \alpha = r_1^2 + r_2^2, \quad \beta = 2r_1 r_2,$$

$$\kappa = 1 + r_1^2 r_2^2, \quad r_1 = \frac{n_l - n_v}{n_l + n_v}, \quad r_2 = \frac{n_s - n_l}{n_s + n_l}. \tag{4}$$

Here, n_v, n_s, and n_l are the refractive indices of vapor, solid, and liquid phases, respectively, and λ is the wavelength of light.

The slope $(d\delta/dx)$ of the thickness profile (local slope angle) and the curvature (K) are obtained at pixel number p by fitting a second-order polynomial (coefficient of regression greater than 0.99) to the thickness at pixel numbers $p-1$, p, and $p+1$. The diameter of a pixel was 0.177 μm. The curvature is calculated using

$$K = \frac{\dfrac{d^2\delta}{dx^2}}{\left[1 + \left(\dfrac{d\delta}{dx}\right)^2\right]^{3/2}} + \frac{\dfrac{d\delta}{dx}}{x\left[1 + \left(\dfrac{d\delta}{dx}\right)^2\right]^{1/2}}. \tag{5}$$

Thus, the technique successfully measures the film thickness and evaluates the slope and curvature at every pixel position. This technique captures the variations of these quantities as a function of position. All the data of the condensing and coalescing drops are analyzed using this technique. Validation of the experimental technique is discussed in the Appendix.

The experimental technique presented here is limited to the measurement of small contact angles ($<13°$). This also limits the measurement of the maximum film thickness to about 4 μm. Also, to obtain the reflectivity images, the difference between the refractive indices of the solid and liquid should be as high as possible. This is because the contrast of the reflectivity images is a function of the refractive indices of the solid and liquid [12].

IV. EXPERIMENTAL OBSERVATIONS

Figures 2(a)–2(d) show the experimentally obtained optical micrographs of the condensing drops during the coalescence process. Figures 2(a) and 2(b) show that the two drops grow in size due to condensation and approach each other, still keeping their symmetric shape intact. Figure 2(c) depicts the merging of the two drops resulting in an elongated asymmetric drop. The drop shape evolves and eventually becomes symmetric [Fig. 2(d)].

A. Profiles of the drops before coalescence

Drops of 2-propanol grow symmetrically before coalescence. Figure 3 shows the data of the measured base radii (R) of the two growing drops as a function of time. The data fit to a straight line with a high degree of accuracy as shown in Fig. 3. This indicates that the drops grow with constant spreading velocities before they merge. The spreading velocities of the larger and smaller drops calculated based on the data presented in Fig. 3 are 0.14 and 0.12 μm/s, respectively. Assuming that the drops have a spherical cap shape before coalescence, Eq. (6) shows that the surface heat flux (q''_{surface}) is proportional to the rate of change of the radius of the drop:

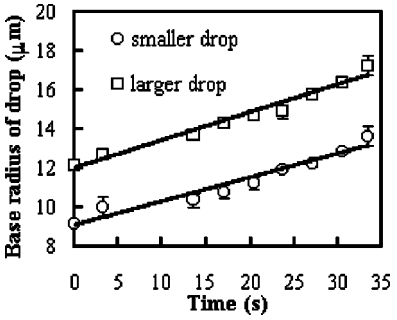

FIG. 3. Base radii of the condensing drops before coalescence.

$$q''_{surface} \propto \frac{\text{volume change rate}}{\text{surface area}} = \frac{2\pi R^2\left(\frac{dR}{dt}\right)}{2\pi R^2} = \frac{dR}{dt}. \quad (6)$$

Hence, the surface heat flux for the larger drop is larger compared to the smaller drop. The difference between the surface heat fluxes of the smaller and larger drops is related to the differences in their contact angles and curvatures, which is discussed below.

The experimentally measured thickness profiles of the two drops [shown in Fig. 2(b)] before merging are shown in Fig. 4(a). The profiles are similar on all the sides of the individual drops, as the drops spread symmetrically before merging. There is a thin flat film adsorbed between the condensing drops. The measured value of the adsorbed film thickness is $\delta_0 = 5.4 \pm 1$ nm and is found to be the same for both the drops. It remains constant as the drops grow and spread during condensation. The corresponding slope angle profiles (a measure of the slope of the profile) are shown in Fig. 4(b). The slope angle ("microscopic varying contact angle") is zero in the adsorbed film region for both drops. The slope angle increases with an increase in the thickness along the drop profile until it passes through a maximum in the contact line region and it is zero at the apex of the drop. If the liquid-vapor interface has constant curvature, the contact angle of a drop can be calculated by fitting the profile of the drop (before coalescence) with a sphere [31] and calculating the slope angle by extrapolating the sphere. However, as is shown from the profiles of the drops in Figs. 4(a) and 4(b), the drop shape is not perfectly spherical. Near the contact line region, the liquid-vapor interface of the drop is concave, and in the thicker portion of the drop, the interface is convex. Thus, the slope angle of the liquid-vapor interface continuously changes as the interface merges with the thin adsorbed flat film on the surface. It has been shown by various researchers [32–37] that the apparent contact angle for a meniscus during phase change cannot be obtained by extrapolation using a constant-curvature model for the interface. For such a case, the "apparent contact angle" is a function of the film thickness. We also observe this phenomenon in the case of the condensing drops of 2-propanol on a quartz surface. Hence we have to define an apparent contact angle at a specific film thickness [35–37] instead of using an extrapolation technique based on the spherical cap model. For

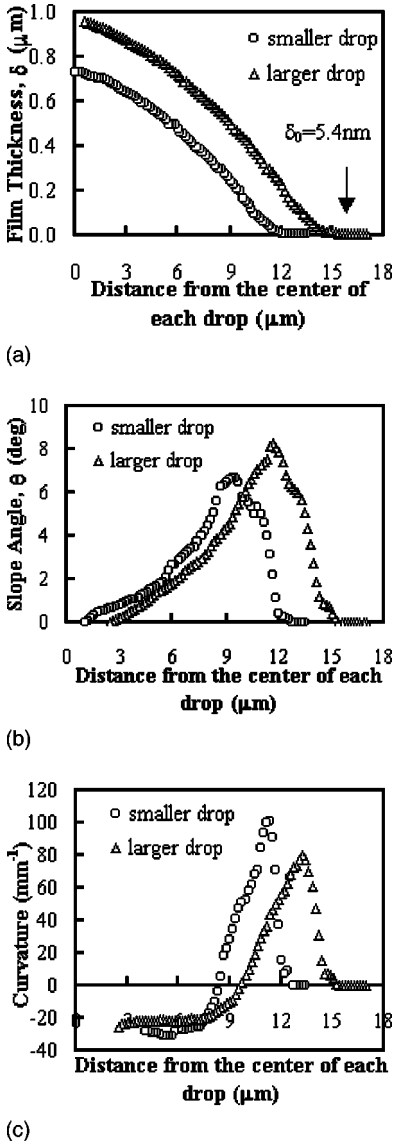

FIG. 4. Film thickness, slope angle, and curvature profiles of the condensing drops [shown in Fig. 2(b)] before coalescence.

convenience and consistency herein, the slope angle at $\delta = 0.098$ μm (zeroth-order interference fringe) is considered to be the apparent contact angle for the drops [13,20]. The apparent contact angles for the smaller and the larger drop are nearly equal (5.3° and 5.6°, respectively). However, the slope angle at the point of inflection, which signifies the start of the contact line region, is lower for the smaller drop (6.6°) than that for the larger drop (8.3°). As demonstrated in previous models, an apparent contact angle is a function of the film thickness [16–18,22,32–34] and needs to be carefully defined. The current results, which give the measured angle as a function of thickness, will aid this definition. In [13] it was found that a higher contact angle gives a higher spreading velocity. The data presented in Fig. 3 agree with this hypothesis.

The curvature profiles calculated using the experimental data and Eq. (5) for the two drops are shown in Fig. 4(c). The curvature is zero in the adsorbed thin-film region. In the

contact line region, it is positive (concave thickness profile) and it increases with an increase in the thickness. It passes through a maximum positive value at $\delta=\delta_{\max}$, and in the thicker portion of the drop, the curvature is negative (convex thickness profile). Thus, the profile of the drop changes from a thin flat film to concave ($K>0$) and then to a convex ($K<0$) profile. The inflection point (maximum positive curvature) represents the interplay between the concave and convex profiles of the drop. The variation in the curvature in the contact line region leads to local capillary flow [16–18,32,36,38]. The curvature at $\delta=0.098$ μm for the smaller drop ($K=6.84\times10^4$ m^{-1}) is lower than that for the larger drop ($K=7.97\times10^4$ m^{-1}). Thus, even though the apparent contact angle at $\delta=0.098$ μm is nearly the same for both the drops, their curvatures (and hence the interfacial pressure fields for fluid flow) are different. However, the maximum in curvature for the smaller drop is higher than that for the larger drop as can be seen from Fig. 4(c). For the smaller drop, the maximum in curvature occurs at a lower film thickness compared to the larger drop. Also, the magnitude of the negative curvature at the apex is more for the smaller drop (-2.85×10^4 m^{-1}) than that for the larger drop (-2.22×10^4 m^{-1}). From Fig. 4(c), at the apex,

$$\frac{K_{smaller\ drop}}{K_{larger\ drop}}=1.28, \tag{7}$$

and from Fig. 3 and Eq. (6),

$$\frac{q''_{surface,\ larger\ drop}}{q''_{surface,\ smaller\ drop}}=\frac{\left(\frac{dR}{dt}\right)_{larger\ drop}}{\left(\frac{dR}{dt}\right)_{smaller\ drop}}=1.17. \tag{8}$$

Equations (7) and (8) show that the ratio of the curvatures of the two drops at the apex matches closely with the ratio of their average surface heat fluxes. Thus, the difference in the average (negative) curvatures of the drops is related to the difference in the spreading velocities and the surface heat fluxes of the two drops. The change in vapor pressure causing condensation is a function of the change in liquid pressure and temperature at the interface: a decrease in vapor pressure at the drop interface due to a decrease in the relative interfacial temperature is partially offset by an increase in vapor pressure due to curvature at the apex [12,13,32,37,39–41]. As the magnitude of the negative curvature at the apex of the smaller drop is more than that of the larger drop, the increase in the interfacial vapor pressure is more for the smaller drop. Thus, the rate of condensation of the larger drop is more than that of the smaller drop. Thus, the experimental technique correctly captures the effect of curvature on surface heat flux and shows the presence of a curvature gradient (pressure gradient) for flow within the condensing drops.

The position of the maximum curvature along the drop identifies a region in the vicinity of the contact line. For the two drops before coalescence, the film thickness at which the maximum curvature occurs ($\delta_{\max}$) and the position of the maximum curvature relative to the center of the drop ($y_{\max}$)

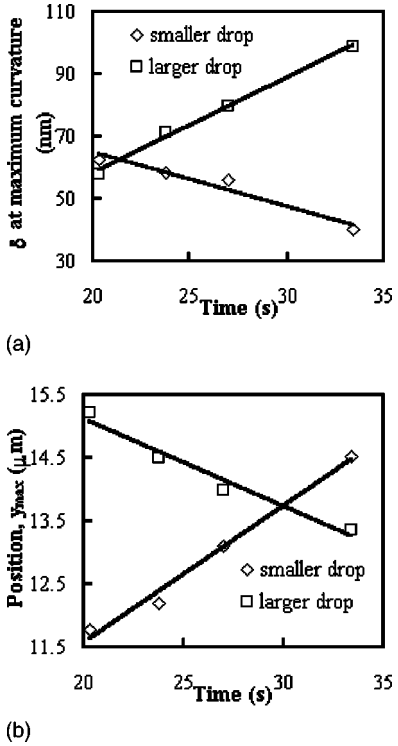

FIG. 5. (a) Film thickness at the location of the maximum curvature for the drops before coalescence as a function of time and (b) positions of maximum curvature ($y_{\max}$) from the center of the two condensing drops before coalescence as a function of time.

are plotted in Figs. 5(a) and 5(b), respectively, as a function of time. Figure 5(a) shows that $\delta_{\max}$ for the smaller drop decreases while that for the larger drop increases as the drops approach each other. Also, from Fig. 5(b), we see that the distance of the location of the maximum curvature from the center of the drop increases for the smaller drop and it decreases for the larger drop during condensation as the two drops approach each other. Thus, the length of the concave region of the smaller drop decreases, while that for the larger drop increases as the drops grow due to condensation before coalescence. These data indicate that the "contact line" of the smaller drop moves towards that of the larger drop. This is also shown by the calculations of the free energy change in the system in a following discussion (Sec. V A). The experimentally obtained profiles of the thickness, slope, and curvature and the presence of the thin adsorbed film and the contact line region in the condensing drops are consistent with previous modeling results [12,15–18,32].

Since the contact angle of the drop before coalescence depends on the velocity of the contact line, we can calculate the line drag coefficient (φ) from the experimental data [42]. The physical reason for the line drag force is that, during the motion of the contact line, there is a dissipation of kinetic energy in the contact line region. We note that the equivalent drag force in our case is not only the effect of viscous flow in the contact line region, as is described in [42], but it is a combined effect of spreading and phase change (condensation) phenomena.

To calculate the line drag coefficient, we define a dynamic balance of forces per unit length of the contact line. When

there is no equivalent drag force, the force balance on a drop at equilibrium is given by

$$\sigma_{lv} \cos \theta_0 + \sigma_{ls} = \sigma_{sv}. \tag{9}$$

Here θ_0 represents the contact angle of the drop in the absence of any drag force. σ_{lv} is the surface tension of the liquid. Due to an equivalent drag force (ω_d), the force balance is modified as

$$\sigma_{lv}\cos \theta_0 + \sigma_{ls} + \omega_d = \sigma_{sv}. \tag{10}$$

The equivalent drag force is expected to be proportional to the velocity of the contact line [42] and is defined as

$$\omega_d = \varphi \frac{dR}{dt}. \tag{11}$$

Here, φ is the line drag coefficient. Since the contact line velocity is positive during condensation, the equivalent drag force is also positive. From Eqs. (9)–(11),

$$\frac{dR}{dt} = -\frac{1}{\varphi}\sigma_{lv}(\cos \theta - \cos \theta_0). \tag{12}$$

Thus, we can calculate the line drag coefficient from a plot of the contact line velocity against the contact angle of the drop. The value of the line drag coefficient calculated based on the experimental data (before coalescence) is 4025.92 Pa s. Based on this value, the drag force (ω_d) is 0.483 mJ/m^2. The value of the drag force is two orders of magnitude less than that of the surface tension force (σ_{lv} cos θ).

B. Coalesced drop: Initial asymmetry of the shape

The instant the two drops touch each other, the smaller drop merges into the larger drop because of the difference in their pressure fields and the resultant drop is asymmetric on its two sides as shown in Fig. 2(c). We note the higher pressure inside the smaller drop at the apex. The experimentally obtained thickness profiles on the two sides of the asymmetric drop are shown in Fig. 6(a). The value of the adsorbed film thickness in the thin-film region of the drop is the same (δ_0=5.4 nm as before) on both the sides. Figure 6(b) shows that the apparent contact angle (at δ=0.098 μm) is the same on the two sides of the drop. In Fig. 6(b), this location corresponds to the relative distances of 3.7 μm for the left edge and 31.8 μm for the right edge of the coalesced drop, respectively. But the maximum in the slope angle is lower at the receding front (left side) of the drop than that at the stationary front (right side). Also from Fig. 6(c), the curvature at δ=0.098 μm and in the contact line region (the inflection point) is lower on the receding front of the drop than that on the stationary front. The curvature profiles represent the capillary pressure within the liquid drop as modeled by the augmented Young-Laplace equation (e.g., [12–14,16]). The difference between the capillary pressures on the receding and the stationary fronts of the coalesced asymmetric drop is the driving force for the shape evolution towards a symmetric shape. This is discussed in Sec. V C.

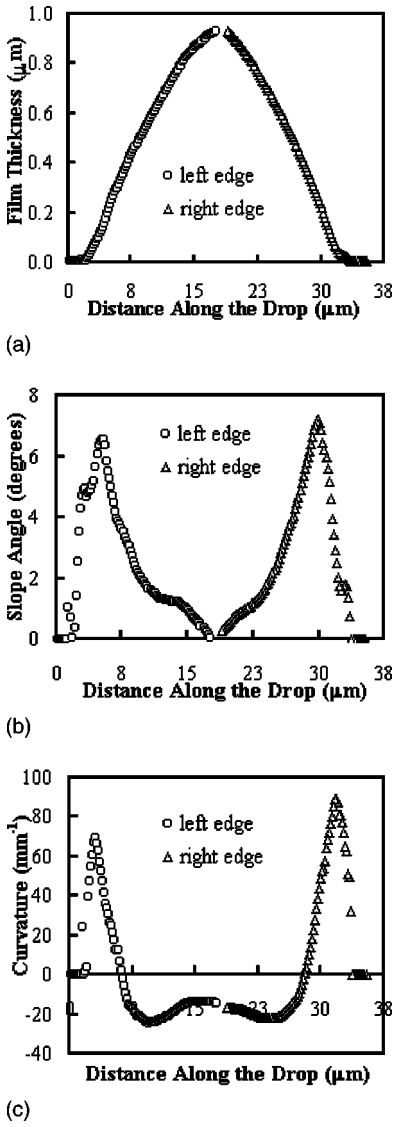

FIG. 6. Film thickness, slope angle, and curvature profiles of the initially asymmetric coalesced drop [shown in Fig. 2(c)] on two sides.

C. Symmetric drop shape

The capillary assisted flow from the receding to the stationary front of the asymmetric drop continues until the drop becomes symmetric in shape as shown in Fig. 2(d). The profiles of the thickness, the slope angle, and the curvature on two sides of the symmetric drop are shown in Figs. 7(a), 7(b), and 7(c), respectively. The values of the apparent contact angle, the curvature at δ=0.098 μm, and also the slope angle and curvature in the contact line region (inflection point) become equal on both the sides of the drop. Thus, the experimental results are consistent with the physical understanding of the completion of the evolution process.

D. Drop size and contact angle during shape evolution

Figures 8 and 9 respectively show the experimentally obtained data of the base radius and the contact angle of the

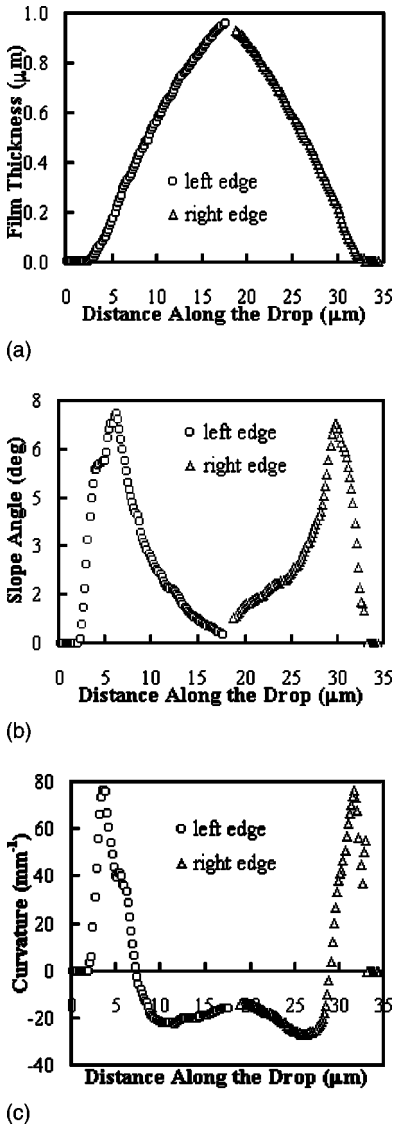

FIG. 7. Film thickness, slope angle, and curvature profiles of the symmetric coalesced drop [shown in Fig. 2(d)] on two sides.

coalesced drop as a function of time during shape evolution of the drop. Figure 8 show the lengths of the major and minor axes of the drop as a function of time, and it show that the coalesced drop is initially asymmetric. As the shape evolves due to fluid flow from the receding to the stationary edge, the length of the major axis decreases, while that of the

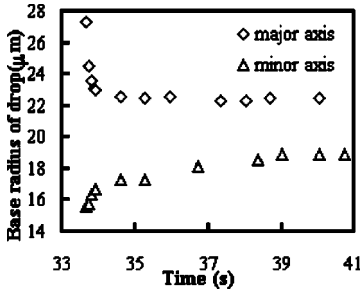

FIG. 8. Base radius of the coalesced drop during shape evolution as a function of time.

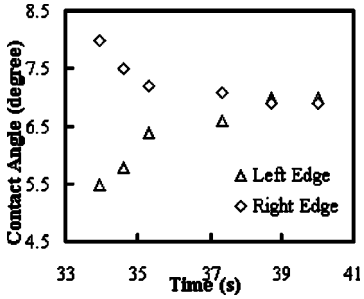

FIG. 9. Contact angle relaxation of the coalesced drop during shape evolution as a function of time.

minor axis increases. Ultimately the two values become constant as the drop becomes more symmetric in shape. The corresponding data of the apparent contact angle in Fig. 9 shows that, just after coalescence, the apparent contact angle at the (receding) left edge is lower than that at the stationary (right) edge. As the drop shape evolves toward a symmetric shape due to the capillary flow, the contact angle at the receding edge increases, while that at the stationary edge decreases. Ultimately, the apparent contact angles at both the edges of the coalesced drop become equal. Thus, the experimental technique provides new details of the dynamics of various parameters during the drop coalescence process.

V. RESULTS AND DISCUSSIONS

A. Driving force for coalescence: Control volume model

The experimental results can be used to obtain a shape-dependent interfacial force field potential for flow. We define a control volume to start at the location of the zeroth dark fringe ($\delta=0.098$ μm) of the smaller drop and end at the zeroth dark fringe of the larger drop. Based on the force balance model of Kim and Wayner [36] with negligible disjoining pressure, the measured interfacial force per unit interline length of the control volume (F) for liquid flow from the smaller drop towards the larger drop is given by

$$F = \sigma_{lv}(\cos\ \theta_2 - \cos\ \theta_1) + \sigma_{lv}\delta(K_2 - K_1). \qquad (13)$$

Here, the subscripts 1 and 2 represent the smaller and larger drops, respectively, σ_{lv} is the surface tension of the liquid ($\sigma_{lv}=20.93\times10^{-3}$ J/m^2), and θ is the apparent contact angle. The thickness δ is the thickness of the film at the ends of the control volume where K and θ are measured at the same values of $\delta=\delta_1=\delta_2$. At $\delta=0.098$ μm, where disjoining pressure is negligible, we get $F=1.2769\times10^{-5}$ N/m just before the drops coalesce [for the drops shown in Fig. 2(b)]. The driving force is directed from the smaller drop towards the larger drop, and it is positive for the experimental data of the apparent contact angles and the curvatures of the two drops. This shows the decrease in the interfacial free energy (per unit area) causing the merger of the smaller drop towards the larger drop. Figure 10 shows the driving force of coalescence per unit length (F) as a function of time as the two drops coalesce. The change in F before $t=33.1$ s is caused by condensation. The data in Fig. 10 show that the driving force per unit length increases as the drops grow. The

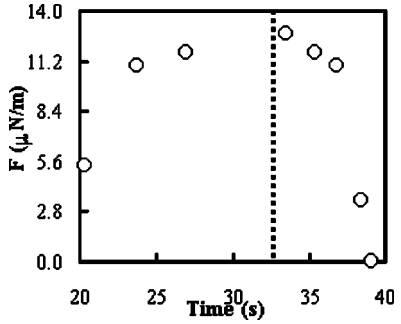

FIG. 10. Driving force for coalescence per unit length (F) as a function of time. The vertical line represents the time of coalescence ($t=33.1$ s).

rate of increase of the driving force for coalescence is higher when the separation between the drops is the largest, and the rate decreases as the two drops approach each other and the separation between them decreases. After the drops coalesce ($t=33.1$ s in Fig. 10), the driving force decreases and ultimately it goes to zero as the coalesced drop evolves from an asymmetric shape into a symmetric shape.

B. Shear stress calculations within each drop just before coalescence: Control volume model

Kim and Wayner [36], Zheng *et al.* [43], and Panchamgam *et al.* [44] developed mathematical models to calculate the average shear stress over a control volume between a meniscus and a thin, flat adsorbed film for a completely wetting system during evaporation. Using the analysis presented in Refs. [36,43,44], we calculate the average shear stress due to fluid flow within a drop for each of the coalescing drops. We define a control volume of length L_{0r}, which can be varied, to start at the location of the adsorbed thin film thickness δ_0 and end at a reference film thickness δ_r along a drop for each drop. The average shear stress (τ_0) over this control volume for an individual drop (just before merging occurs) is defined using the equation

$$\tau_0 = \frac{\sigma_{lv}(\cos\,\theta_r + K_r\delta_r - 1) + \Pi_r\delta_r - \Pi_0\delta_0}{L_{0r}}. \qquad (14)$$

Here, θ_r and K_r are the values of the slope angle and curvature, respectively, at the reference film thickness δ_r. In this equation, the average shear stress exerted by the solid on the liquid within the drop is assumed to be positive if flow is away from the adsorbed thin film.

Using the experimental data of the film thickness, curvature, and slope contact angle at every pixel location along the drops, we calculate the average shear stress over a length L_{0r}. We vary the length of the control volume (L_{0r}) by taking different pixel locations along the drop profile. Figure 11 shows the calculated data of the average shear stress as a function of the reference film thickness (δ_r) along the individual drops just before the coalescence occurs. The results in Fig. 11 show that for film thickness $\delta \leqslant 30$ nm, the average shear stress on the liquid is negative (directed away from the thin film) and equal for both the smaller and larger drops

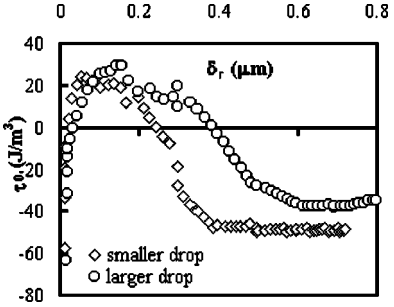

FIG. 11. Average shear stress (τ_0) as a function of the reference film thickness (δ_r) along the coalescing drops.

because in this region, τ_0 is mainly dependent on the disjoining pressure term and the contributions from the curvature and contact angle terms are negligible. Therefore, flow is towards the adsorbed thin film in the region $\delta \leqslant 30$ nm. As the length of the control volume (or δ_r) increases, τ_0 goes through a maximum positive value (at about 60 nm for the smaller drop and 155 nm for the larger drop) and then it goes to a constant negative value for higher values of δ_r (constant convex curvature region). The average stress is positive (directed toward the thin film showing flow away from the adsorbed thin film) for 30 nm $\leqslant \delta \leqslant 0.24$ μm for the smaller drop and for 30 nm $\leqslant \delta \leqslant 0.38$ μm for the larger drop. The change in the sign of the average shear stress in this region indicates that there is a complex flow pattern within the drop near the contact line region as the drops spread during condensation.

A higher value of δ_r represents a control volume that encompasses a region from the thin adsorbed film to the center of the drop. The average shear stress for higher values of δ_r is negative, which indicates a net flow away from the center of the drop as is expected for a spreading drop. From Fig. 11 we see that τ_0 for a higher value of δ_r is more negative for the smaller drop compared to the larger drop. This indicates that there is a potential for net fluid flow from the smaller drop towards the larger drop before coalescence, which is not obvious. This flow is governed by the slope angle, curvature, and disjoining pressure of the two coalescing drops. Thus, the calculation of the average shear stress gives an enhanced physical understanding of the spreading and coalescence of the drops.

C. Driving force for shape evolution

After the drops coalesce, the initial drop is asymmetric in shape as shown above in the experimental results of Sec. IV B. We demonstrate that the drop evolves into a symmetric shape due to capillary flow within the drop. The asymmetry of the coalesced drop and the kinetics of relaxation of the drop towards a symmetric shape were studied by Andrieu *et al.* [1] and Nikolayev and Beysens [4]. Here, we explain the observed asymmetry of the coalesced drop and its relaxation using the curvature gradient and the resulting capillary flow within the drop as the left side of the coalesced drop recedes towards the right front.

The curvature profiles represent the capillary pressure within the liquid drop as modeled by the augmented Young-Laplace equation (e.g., [12–14,16])

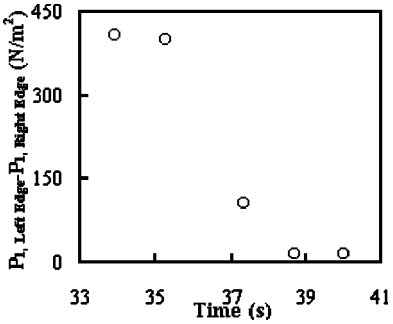

FIG. 12. Difference between the liquid pressures on the two sides of the coalesced drop during shape evolution as a function of time.

$$P_v - P_l = K\sigma_{lv} - \frac{A}{6\pi\delta^3}, \tag{15}$$

where P_v is the vapor pressure, P_l is the liquid pressure, and A is the nonretarded Hamaker constant. The value of the Hamaker constant is calculated to be -5.57×10^{-21} J [14] based on the refractive indices and the dielectric constants of the three phases involved. The first term on the right-hand side of Eq. (15) represents the capillary force while the second term represents the dispersion force due to a van der Waals interaction, which becomes negligibly small for $\delta > 100$ nm. Thus, near the inflection point, the main contribution to the liquid pressure within the drop is from the capillary force. The lower (positive) value of the concave curvature [shown in Fig. 6(c)] near the contact line region of the receding front of the drop signifies a higher liquid pressure (P_l) compared to the stationary front. Thus, there is a capillary flow of the liquid from the receding front to the stationary front within the coalesced drop. The driving force for the shape evolution of the coalesced drop, which is the difference between the liquid pressures at the left (receding front) and right edges (stationary front) of the coalesced drop, calculated using Eq. (15) at the inflection point, is shown in Fig. 12 as a function of time. The data in Fig. 12 show that the difference in the liquid pressures is maximum just after the drops coalesce and the shape of the drop is asymmetric. As the shape of the drop evolves toward a symmetric shape, the difference in the liquid pressures, which causes the shape evolution, decreases. Thus, the driving force for the liquid flow from the receding front toward the stationary front decreases as the asymmetry in the shape of the coalesced drop decreases. Ultimately the liquid pressures on both the sides of the coalesced drop become equal when the coalesced drop evolves into a symmetric shape. Thus, the evaluated pressure field is consistent with the shape evolution of the coalesced drop.

D. Center-of-mass calculations

The experimental data is also used to analyze the positions of the center of mass of the drops during the coalescence process. The positions of the center of mass of the two drops before coalescence are calculated based on the experimental data of the contact area of the drops. The centers of mass of the two drops do not move before coalescence. For the coalesced drop, the position of the center of mass (X_3, Y_3) is calculated using Eqs. (16) and (17), which are based on the two-dimensional formulation of Andrieu *et al.* [1]:

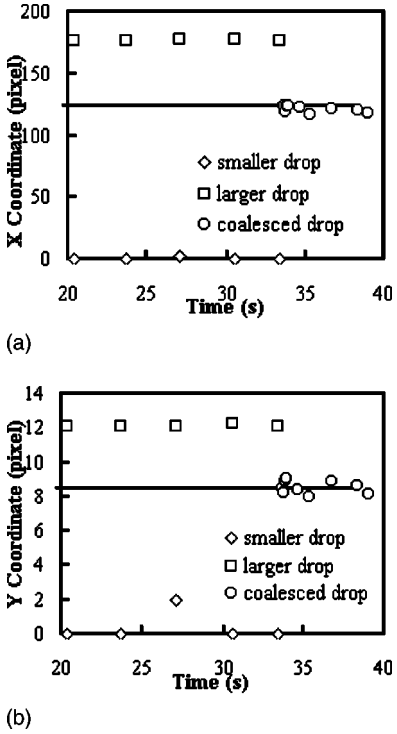

FIG. 13. (a) Pixel position of the X coordinate of the center of mass. The straight line shows the value calculated using Eq. (16). The pixel position of 0 corresponds to the position of the X coordinate of the smaller drop. (b) Pixel position of the Y coordinate of the center of mass. The straight line shows the value calculated using Eq. (17). The pixel position of 0 corresponds to the position of the Y coordinate of the smaller drop.

$$X_3 = \frac{X_1R_1^3 + X_2R_2^3}{R_1^3 + R_2^3}, \tag{16}$$

$$Y_3 = \frac{Y_1R_1^3 + Y_2R_2^3}{R_1^3 + R_2^3}, \tag{17}$$

where X, Y, and R are the coordinates and radii of the smaller drop (subscript 1) and the larger (subscript 2) drop.

Figures 13(a) and 13(b) show the positions of X and Y coordinates of the center of mass of the two drops before coalescence and also those of the coalesced drop as a function of time. The points in Fig. 13 show the experimentally obtained positions of the center of mass, and the lines show the positions calculated based on Eqs. (16) and (17). Figure 13 shows that the experimental data closely agree with the calculations based on Eqs. (16) and (17). Also, the position of the center of mass of the coalesced drop is closer to that of

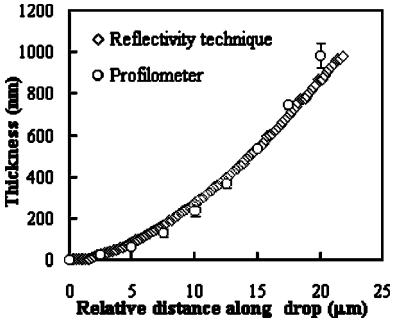

FIG. 14. Thickness profiles of the concave region of a drop of polydimethylsiloxane (PDMS) on a glass surface obtained from the reflectivity technique and profilometry. The maximum error between the thicknesses obtained from the two measurements is 6%.

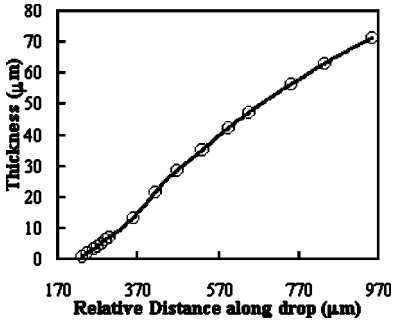

FIG. 15. Profile of a PDMS drop on a glass surface obtained with profilometry up to a region near the center of the drop. The solid line is a guide for the eye.

the larger drop. This is consistent with the experimental observation that the smaller drop merges toward the larger drop. This was also shown by the force balance calculations [Eq. (13)] based on the experimentally obtained interfacial parameters, which showed that the liquid from the smaller drop flows toward the larger drop.

E. Generality of the mechanisms

The coalescence phenomena and the dynamics of various parameters (thickness profile, slope angle, curvature profile, and positions of the center of mass) during coalescence, reported here, are applicable to small contact angle systems. Also, the results reported in the paper are for a pure liquid, 2-propanol. Following are some of the factors, which would alter the spreading and coalescence mechanisms.

(a) The presence of a surfactant (or another component in the liquid) would create a surface tension gradient, and the results would be different. In the case of surfactant drops, the contact angle would not remain constant during the growth of the drops. This work is currently in progress.

(b) If the surface has defects, the contact line is pinned in a metastable state. Therefore, relaxation of drops is more rapid than that on an ideally clean surface [4].

(c) (For drops having higher contact angles, the relaxation time would be shorter. In general, as the contact angle increases, the relaxation time of the coalesced drop decreases [1,4]. This is because the driving force for relaxation increases with an increase in the contact angle.

(d) The coalescence phenomena and coalescence time are functions of the *p*H of the liquid. The presence of the electrostatic double-layer forces alters the van der Waals forces on the thin film between the drops and hence the coalescence time [5,6]. But this is not an issue for a pure organic liquid (2-propanol) studied here.

(e) The coalescence time and the relaxation time of the coalesced drop depend on the initial kinetic energy given to the drop [45]. This depends on the manner in which the drops are made to coalesce. For example, syringe deposition of drops induces oscillations of the drops. In [45], the coalescence between two drops deposited close to each other occurs when a small drop is deposited on the top of one of the drops. Strong oscillations of the liquid-vapor interface of the composite drop occur due to the impact with the newly added drop. Due to the oscillations, the drop surface pulls the contact line, which accelerates its motion. However, the drop oscillations are not observed for the case of coalescence during condensation [45]. This is also the case in our experiments, as the drops coalesce due to spreading induced by condensation.

VI. CONCLUSIONS

The details of the growth and coalescence of two condensing drops of 2-propanol are obtained experimentally by measuring the evolution of the thickness profiles. The results show the presence of a thin flat film adjacent to the condensing drops, and the adsorbed film thickness is found to be constant and independent of the point of measurement. Even though the apparent contact angle at the film thickness $\delta = 0.098$ μm is nearly the same for both drops before coalescence, their curvatures (and hence the interfacial pressure fields) are different. The centers of mass of the two drops do not move before coalescence. The pressure field indicates that there are complex flow patterns in the flow field. We measure the details of the drop coalescence process and show that liquid flow from the smaller drop towards the larger drop is due to the difference in their shape-dependent pressure fields. This was also shown by the calculation of the evolution of the center of mass of the two coalescing drops. The curvature and its gradient describe the process more completely than only the average curvature and the contact angle.

The asymmetric coalesced drop self-adjusts and evolves into a symmetric shape due to the capillary flow within the drop. The calculated pressure field in the coalesced, asymmetric drop is consistent with the required capillary assisted flow from the receding to the stationary front of the asymmetric drop, until it becomes symmetric. Using a control volume model the calculation of the shear stress also explains the physics of fluid flow during coalescence. The experimental results give new insights into the phenomenon of coalescence of drops and explain the significance of the capillary pressure gradient in the contact line region in governing the process.

ACKNOWLEDGMENT

This material is based on the work supported by the National Aeronautics and Space Administration under Grant No. NAG3-2383.

APPENDIX: TECHNIQUE VALIDATION

To validate the accuracy of the measurement of the profiles, we deposited a drop of a polymer, polydimethysiloxane (PDMS) (Sylgard 184 from Dow Corning) on a clean microscope glass slide with a micropipette. The polymer drop was cured by heating the sample to 60 °C for 3 h in an oven. The drop solidified after curing. The profile of the drop was then measured using the reflectivity technique described in the paper. Since the drop had a large diameter (3000 μm), we could analyze only the concave region of the drop (up to $\delta = 1$ μm) with our technique. This is because the separation between the interference fringes decreases as the profile becomes steep. The same drop was then analyzed with a profilometer (Alpha Step 200 from Tencor). The thickness profiles of the drop obtained from the profilometer and the reflectivity technique are presented in Fig. 14. Figure 14 clearly shows that the experimental thickness profile obtained from the reflectivity analysis agrees with the data obtained from the profilometry measurements. The maximum error between the thicknesses obtained from the two measurements is 6% in the thicker region (δ=1000 nm). Also, the contact angle of the drop of PDMS on the glass surface obtained from the reflectivity analysis (1.8°) is very close to that obtained from the profilometry data (1.7°). Thus, the experimental technique based on the reflectivity analysis accurately measures the profiles of the drops. Figure 15 shows the profile of the PDMS drop obtained with profilometry up to a region near the center of the drop. Figure 15 clearly shows the transition from concave to convex shape of the drop, which is also observed in our results of the condensing drops (Fig. 4) of 2-propanol on a quartz surface. Thus, the results from the profilometry measurements also validate the presence of both concave and convex regions in the profile of a drop having a small contact angle.

[1] C. Andrieu, D. A. Beysens, V. S. Nikolayev, and Y. Pomeau, J. Fluid Mech. **453**, 427 (2002).
[2] A. Menchaca-Rocha, A. Martínez-Dávalos, R. Núñez, S. Popinet, and S. Zaleski, Phys. Rev. E **63**, 046309 (2001).
[3] B. Pu and D. Chen, J. Colloid Interface Sci. **235**, 1 (2001).
[4] V. S. Nikolayev and D. A. Beysens, Phys. Rev. E **65**, 046135 (2002).
[5] D. Li, J. Colloid Interface Sci. **163**, 108 (1994).
[6] S. R. Deshikan and K. D. Papadopoulos, J. Colloid Interface Sci. **174**, 302 (1995).
[7] Y. Amarouchene, G. Cristobal, and H. Kellay, Phys. Rev. Lett. **87**, 206104 (2001).
[8] I. B. Ivanov, K. D. Danov, and P. A. Kralchevsky, Colloids Surf., A **152**, 161 (1999).
[9] S. M. Yang, L. G. Leal, and Y. S. Kim, Jr., J. Colloid Interface Sci. **250**, 457 (2002).
[10] A. Sharma and E. Ruckenstein, Colloid Polym. Sci. **266**, 60 (1988).
[11] B. V. Derjaguin and Z. M. Zorin (unpublished).
[12] S. DasGupta, J. L. Plawsky, and P. C. Wayner, Jr., AIChE J. **41**, 2140 (1995).
[13] S. J. Gokhale, J. L. Plawsky, and P. C. Wayner, Jr., J. Colloid Interface Sci. **259**, 354 (2003).
[14] S. J. Gokhale, J. L. Plawsky, P. C. Wayner, Jr., and S. DasGupta, Phys. Fluids **16**, 1942 (2004).
[15] P. G. de Gennes, Rev. Mod. Phys. **57**, 827 (1985).
[16] P. C. Wayner, Jr., J. Colloid Interface Sci. **77**, 495 (1980).
[17] D. M. Anderson and S. H. Davis, Phys. Fluids **7**, 248 (1995).
[18] L M. Hocking, Phys. Fluids **7**, 2950 (1995).
[19] N. V. Churaev, N. E. Esipova, R. M. Hill, V. D. Sobolev, V. M. Starov, and Z. M. Zorin, Langmuir **17**, 1338 (2001).
[20] S. J. Gokhale, J. L. Plawsky, and P. C. Wayner, Jr., Adv. Colloid Interface Sci. **104**, 175 (2003).
[21] G. Wiegand, T. Jaworek, G. Wegner, and E. Sackmann, J. Colloid Interface Sci. **196**, 299 (1997).
[22] T. D. Blake, J. Chem. Soc., Faraday Trans. 1 **71**, 192 (1975).
[23] F. Renk, P. C. Wayner, Jr., and G. M. Homsy, J. Colloid Interface Sci. **67**, 408 (1978).
[24] F. J. Renk and P. C. Wayner, Jr., J. Heat Transfer **101**, 55 (1979).
[25] J. G. Truong and P. C. Wayner, Jr., J. Chem. Phys. **87**, 4180 (1987).
[26] A. H. Liu, P. C. Wayner, Jr., and J. L. Plawsky, Phys. Fluids **6**, 1963 (1994).
[27] Y.-X. Wang, J. L. Plawsky, and P. C. Wayner, Jr., Microscale Thermophys. Eng. **5**, 55 (2001).
[28] L. Zheng, Y.-X. Wang, J. L. Plawsky, and P. C. Wayner, Jr., Int. J. Heat Mass Transfer **45**, 2021 (2002).
[29] L. Zheng, Y.-X. Wang, J. L. Plawsky, and P. C. Wayner, Jr., Langmuir **18**, 5170 (2002).
[30] J. D. Chen and N. Wada, J. Colloid Interface Sci. **148**, 207 (1992).
[31] I. B. Ivanov and B. V. Toshev, Colloid Polym. Sci. **253**, 593 (1975).
[32] M. Potash and P. C. Wayner, Jr., Int. J. Heat Mass Transfer **15**, 1851 (1972).
[33] B. V. Deryagin, V. M. Starov, and N. V. Churaev, Colloid J. USSR **38**, 875 (1976).
[34] Y. Solomentsev and L. R. White, J. Colloid Interface Sci. **218**, 122 (1999).
[35] S. J. S. Morris, J. Fluid Mech. **432**, 1 (2001).
[36] I. Y. Kim and P. C. Wayner, Jr., J. Thermophys. Heat Transfer **10**, 320 (1996).
[37] S. DasGupta, I. Y. Kim, and P. C. Wayner, Jr., J. Heat Transfer **116**, 1007 (1994).
[38] M. E. R. Shanahan, Langmuir **17**, 8229 (2001).
[39] P. C. Wayner, Jr., Y. K. Kao, and L. V. La Croix, Int. J. Heat Mass Transfer **19**, 487 (1976).
[40] S. Moosman and G. M. Homsy, J. Colloid Interface Sci. **73**, 212 (1980).

[41] P. C. Wayner, Jr., Colloids Surf., A **89**, 89 (1994).
[42] V. L. Kolev, I. I. Kochijashky, K. D. Danov, P. A. Kralchevsky, G. Broze, and A. Mehreteab, J. Colloid Interface Sci. **257**, 357 (2003).
[43] L. Zheng, J. L. Plawsky, P. C. Wayner, Jr., and S. DasGupta, J. Heat Transfer **126**, 169 (2004).
[44] S. S. Panchamgam, S. J. Gokhale, J. L. Plawsky, S. DasGupta, and P. C. Wayner, Jr. (unpublished).
[45] R. Narhe, D. Beysens, and V. S. Nikolayev, Langmuir **20**, 1213 (2004).